Structure, Volume *29*

Supplemental Information

Unveiling the polarity of actin filaments by cryo-electron tomography

Bruno Martins, Simona Sorrentino, Wen-Lu Chung, Meltem Tatli, Ohad Medalia, and Matthias Eibauer

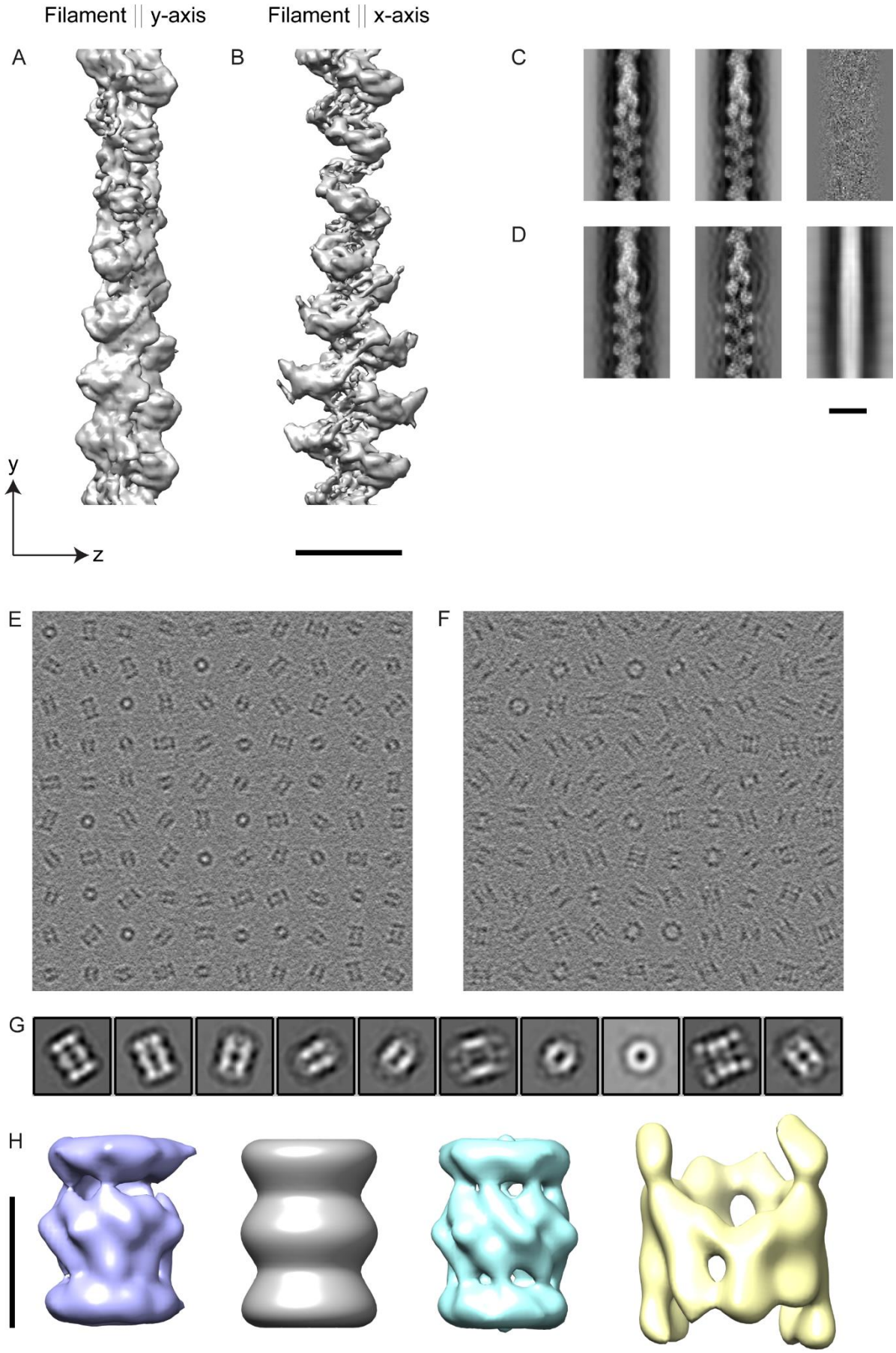
Filament || y-axis
Filament || x-axis
A
B
C
D
y
z
E
F
G
H
Refine3D
Reference
Class3D/class#1
Class3D/class#2

Figure S1. Structural analysis of projected subtomograms by single particle methods. Related to Figure 1. (**A**) Structure of an actin filament (EMD-6179 (Galkin et al., 2015)), that was oriented parallel to the tilt-axis (y-axis), and then distorted by the missing wedge. (**B**) However, if the filament was oriented parallel to the x-axis (orthogonal to the tilt-axis), the anisotropic distortion caused by the missing wedge in z-direction is substantially more pronounced. (**C**) Left to right: projection of filament (**A**) in z-direction, projection of filament (**B**) in z-direction, and difference image between the two projections. The difference image is featureless, which indicates that the missing wedge induced anisotropy vanishes in the projection images. (**D**) However, if a mask in z-direction is applied before projection (in this case the height of the mask was 11 nm), the difference image is not featureless anymore. The influence of this mask on the precision of APT is part of the validation of the method. Scale bars 10 nm.

We tested our approach for subtomogram averaging with a dataset of modelled subtomograms (Forster et al., 2008), including missing wedge (tilt-range from -60° to +60°), contrast transfer function (defocus of -6 µm, acceleration voltage 300 kV, spherical aberration 2.0 mm, pixelsize 0.42 nm), and modulation transfer function. The dataset contains two particle species: 2048 20S-proteasomes (PDB-1PMA (Lowe et al., 1995)) and 256 thermosomes (PDB-1A6D (Ditzel et al., 1998)). The orientation of the particles was uniformly distributed over the 3D rotation space, and both subtomogram species were modelled with a SNR = 10^{-1}. The subtomograms were projected without masking in z-direction. (**E**) A gallery of 100 projected proteasomes is displayed. (**F**) A gallery of 100 projected thermosomes is shown. (**G**) The projected images of both particle species were mixed and a 2D classification in RELION (Scheres, 2012) was performed. Since the number of proteasome particles is eight-fold higher than thermosome particles, most of the classes are dominated by proteasomes. (**H**) For 3D reconstruction we initially executed a 3D refinement job in RELION. As starting reference, the proteasome structure was filtered to 45 Å resolution and rotationally symmetrized along the z-axis (grey structure). The obtained reconstruction is shown on the left (blue structure). It resembles a proteasome to a certain degree, but the structure is obviously distorted by the thermosome

fraction. Then we performed a 3D classification job in RELION, using the same starting reference as previously, and assuming two classes. Both particle species were properly separated in 3D, with no classification error as compared to the ground truth – all proteasomes were assigned to class#1, cyan structure, and all thermosomes to class#2, yellow structure. The proteasome class average shows the expected D7 symmetry. Scale bar 10 nm.

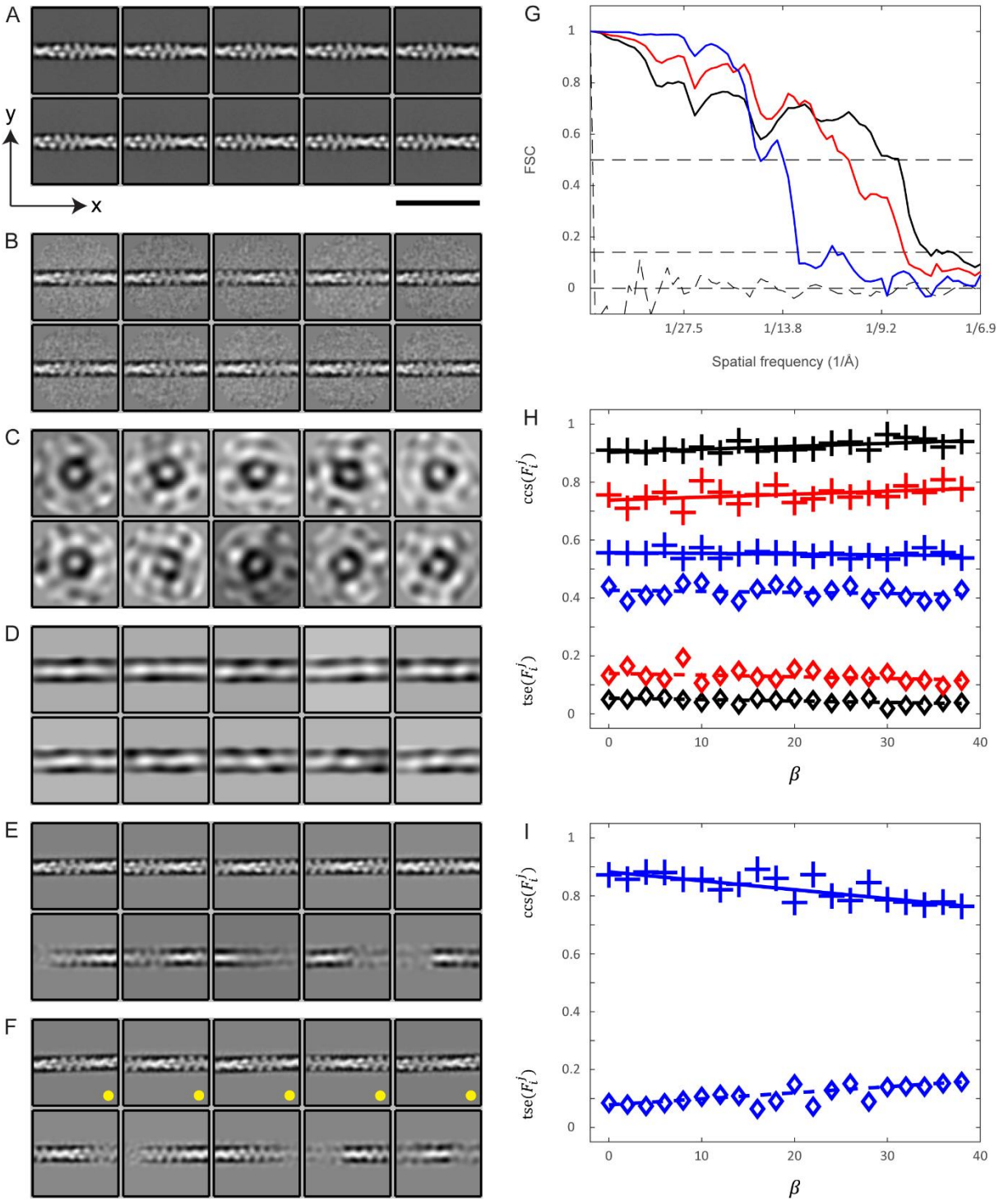

Figure S2. Processing of modelled actin bundles. Related to Figure 1. (**A**) The aim of the prealignment step (*Step IV*) is to orient the (central) filament density in the projected subtomograms parallel to the x-axis. Therefore, we used a template library, which was created from an actin filament structure by successively rotating and projecting the filament. The image

shows the first ten entries in the template library. Scale bar 50 nm. (**B**) The first ten class averages after ten iterations of prealignment are shown. The particle rotations and translations were used as priors for the next step. (**C**) The 2D classification module (*Step V*) of APT aims to produce high quality class averages with RELION (Scheres, 2012). Therefore, we employ the prealignment priors, which allow to apply a mask parallel to the filament during 2D classification. This mask diminishes the influence of neighboring filaments. In contrast to the prealignment step, it is vital that this 2D classification is unsupervised. This ensures that as much as possible structural heterogeneity can cluster in a data-driven way into distinct class averages. The first ten class averages of the zeroth iteration are shown. It illustrates the initialization of the unsupervised 2D classification. (**D**) In the first iteration the applied mask appears, and the prealignment priors force the central filament density parallel to the x-axis. (**E**) After ten iterations of unsupervised 2D classification the class averages capture most of the structural heterogeneity present in the dataset. (**F**) After 100 iterations we selected the segments, which were assigned to the class averages marked with yellow dots, for subsequent 3D reconstruction (*Step VI*).

(**G**) Based on three modelled datasets (SNRs of 10^{-2}, 10^{-3}, and 10^{-4}), each with varying bundle orientation α, but no bundle tilt ($\beta = 0°$), we reconstructed three actin filament structures (~ 10'000 segments per average). Resolution was estimated by Fourier shell correlation (FSC), calculated between the averages and EMD-6179 (Galkin et al., 2015), using the 0.5 threshold criterion (Rosenthal and Henderson, 2003). Prior FSC computation, the structures were aligned with each other. As expected, the resolution values drop with decreasing SNR, 9 Å (black FSC curve, SNR = 10^{-2}), 10 Å (red FSC curve, SNR = 10^{-3}), and 16 Å (blue FSC curve, SNR = 10^{-4}). The dashed curve is the FSC between two noise volumes, using an identical masking as for the resolution estimation of the averaged structures. It shows that the mask has no inflating effect on the resolution. (**H**) APT workflow was applied to three modelled datasets (same SNRs as before), each with varying bundle tilt β between $0°$ to $38°$, but fixed bundle orientation ($\alpha = 0°$). The projection thickness parameter was set to 44 nm for all

segments. In the plot, the averaged $\mathrm{ccs}(F_i^j)$ values per bundle are shown as cross symbols (black, red, and blue correspond to SNR of 10^{-2}, 10^{-3}, and 10^{-4}). Slopes of the solid black, red, and blue linear regression lines are $1.04 \cdot 10^{-3} \pm 3.04 \cdot 10^{-4}$, $1.03 \cdot 10^{-3} \pm 5.54 \cdot 10^{-4}$, and $-2.63 \cdot 10^{-4} \pm 2.78 \cdot 10^{-4}$, and p values of the slopes are 0.0032, 0.08, and 0.36, respectively. The averaged $\mathrm{tse}(F_i^j)$ values per bundle are shown as diamond symbols. The mean values per SNR condition are 0.04 ± 0.01 (SNR = 10^{-2}), 0.13 ± 0.02 (SNR = 10^{-3}), and 0.42 ± 0.02 (SNR = 10^{-4}). (**l**) We conducted the APT workflow on an additional dataset with SNR = 10^{-4} and varying bundle tilt β. However, here we assumed that the bundle tilt is known a priori. Consequently, it is possible to adapt the projection mask for each segment individually, which allows to revert the projection thickness to 11 nm. The averaged $\mathrm{ccs}(F_i^j)$ values per modelled bundle are shown as blue crosses. The slope of the solid blue linear regression line is $-3.07 \cdot 10^{-3} \pm 5.49 \cdot 10^{-4}$ and the p value of the slope is $2.62 \cdot 10^{-5}$. The averaged $\mathrm{tse}(F_i^j)$ values per bundle are shown as blue diamond symbols with a mean value of 0.11 ± 0.03.

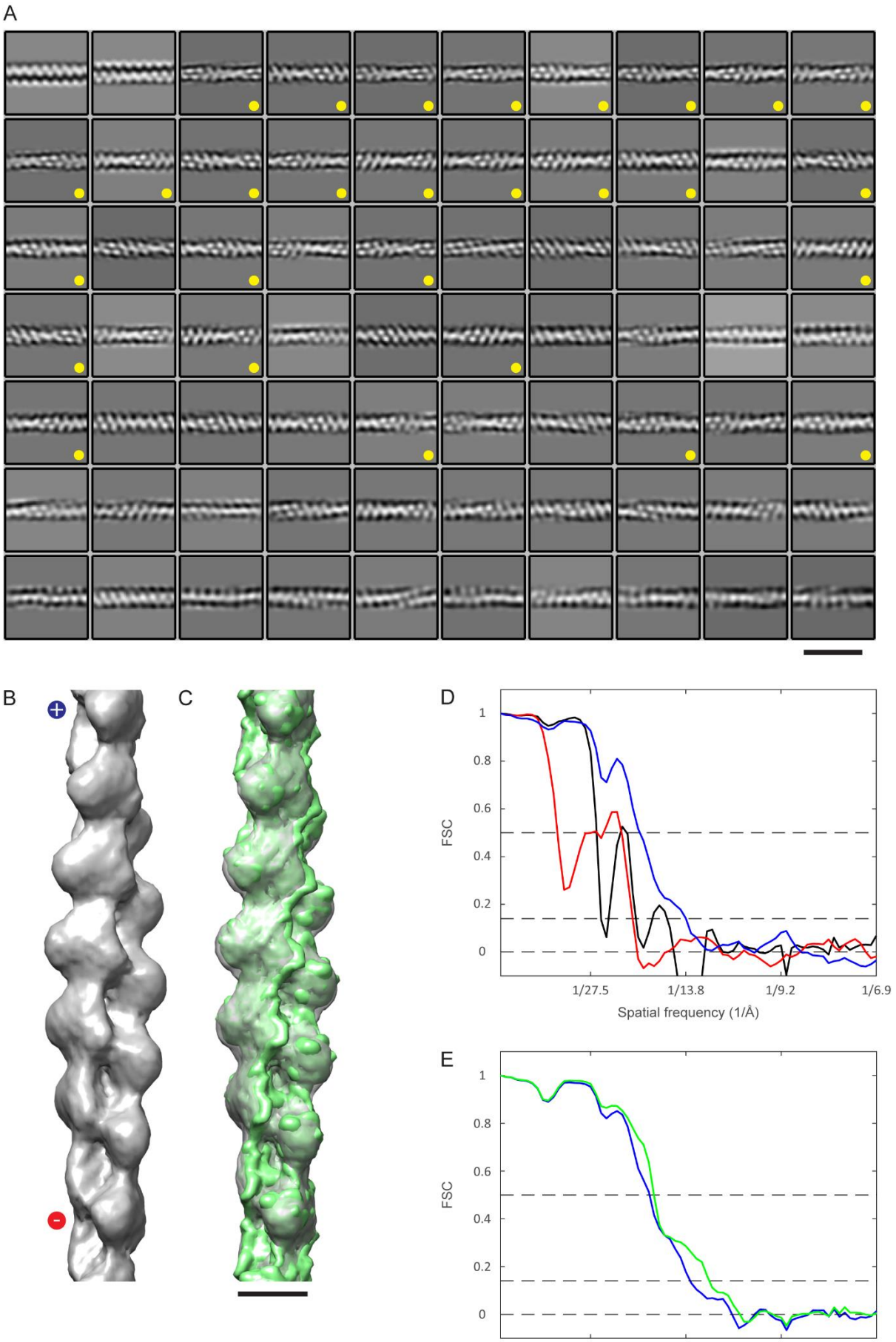
A
B
C
D
FSC
1
0.8
0.6
0.4
0.2
0
1/27.5
1/13.8
1/9.2
1/6.9
Spatial frequency (1/Å)
E
FSC
1
0.8
0.6
0.4
0.2
0
1/27.5
1/13.8
1/9.2
1/6.9
Spatial frequency (1/Å)

Figure S3. In-situ actin filament average from manually segmented actin bundles. Related to Figure 2. (**A**) The image shows the final class averages of the 2D classification (*Step V*). Those segments, which were combined to class averages marked with yellow dots, were selected for 3D reconstruction (20'585 segments out of 43'400). Scale bar 36 nm. (**B**) In-situ actin filament structure, reconstructed from selected segments (*Step VI*). The average shows clear polar features, and the position of the plus-end can be detected unambiguously (plus and minus symbols). (**C**) Here we docked EMD-6179 (Galkin et al., 2015) (green isosurface) into our structure (grey isosurface), reaching a correlation value of 0.87. However, if we reverse the filament direction the correlation value drops to 0.73. This shows that the average exhibits polar features. Scale bar 5 nm. (**D**) Resolution was estimated by FSC, calculated between the obtained in-situ average and EMD-6179, serving as an external reference. Prior FSC computation the structures were aligned with each other. The corresponding blue FSC curve crosses the 0.5 threshold criterion (Rosenthal and Henderson, 2003) at 18 Å. The black FSC curve was calculated between the 3D reconstruction template and EMD-6179. In comparison with the blue FSC curve it proofs that during 3D reconstruction higher resolution features were successfully extracted from the data (no template bias). The red FSC curve was calculated between the obtained in-situ average and EMD-6179, however, the docking prior FSC computation was conducted with a reversed filament direction compared to the external reference. (**E**) Based on extracted filaments (2146 at this stage) another particle set was created. It only contains those 9931 segments with polarity labels that are congruent with polarity labels of the respective filaments. Based on these segments a Refine3D job was performed in RELION (Scheres, 2012), with local searches of helical symmetry. The resolution of this structure (17 Å) was measured as described in (**D**). The corresponding FSC is plotted as green curve in (**E**). The structure is deposited in the Electron Microscopy Data Bank under accession code EMD-11976. For comparison we added the blue FSC curve, which is based on a structure, reconstructed with identical parameter and particle number (9931 segments), but the segments were randomly selected from yellow dotted classes in (**A**).

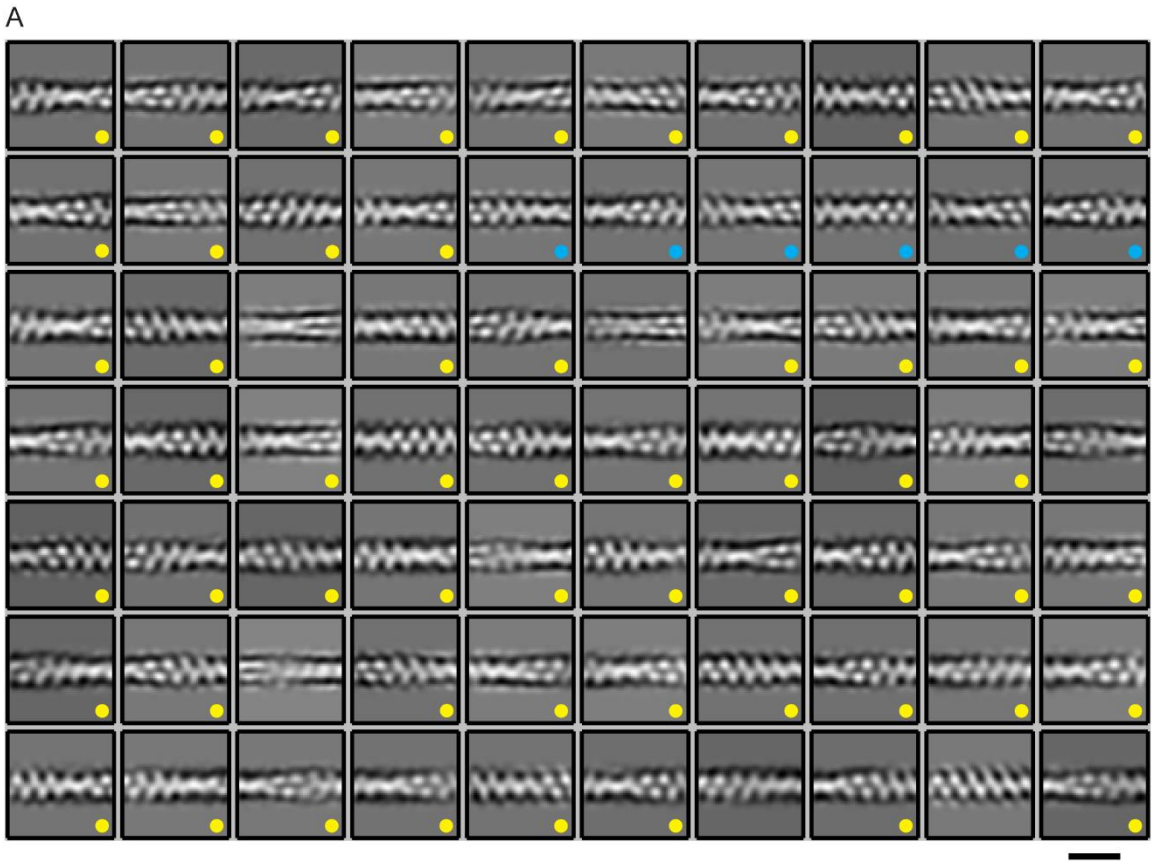
A
B
C
D
E
F
G

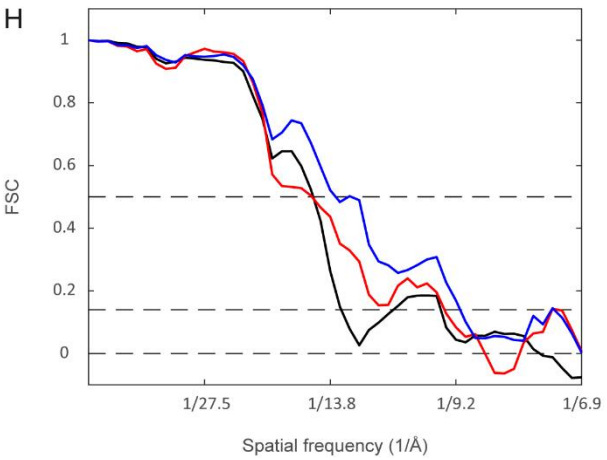
H
FSC
1
0.8
0.6
0.4
0.2
0
1/27.5
1/13.8
1/9.2
1/6.9
Spatial frequency (1/Å)

Figure S4. Processing of automatically segmented actin bundles. Related to Figure 2. (**A**) The image shows the final class averages (*Step V*). Those segments, which were combined to class averages marked with yellow dots, were selected for 3D reconstruction (72'973 segments out of 247'940). The class averages marked with blue dots are also shown in Figure 2D. Scale bar 18 nm. The three class averages (**B**), (**D**), and (**F**) are shown as grey isosurfaces. In (**C**), (**E**), and (**G**) we docked EMD-6179 (Galkin et al., 2015) (green isosurfaces) into the respective structures. Class average (**B**) and docking (**C**) are also displayed in Figures 2E and Figure 2F, respectively. Scale bar 5 nm. (**H**) Resolution was estimated by FSC, calculated between obtained in-situ class averages and EMD-6179 (Galkin et al., 2015), serving as an external reference. Prior FSC computation structures were aligned to each other. The corresponding red FSC curve (class#3, (**F**)), black FSC curve (class#2, (**D**)), and blue FSC curve (class#1, (**B**)) cross the 0.5 threshold criterion (Rosenthal and Henderson, 2003) at 15 Å, 15 Å, and 14 Å resolution, respectively.

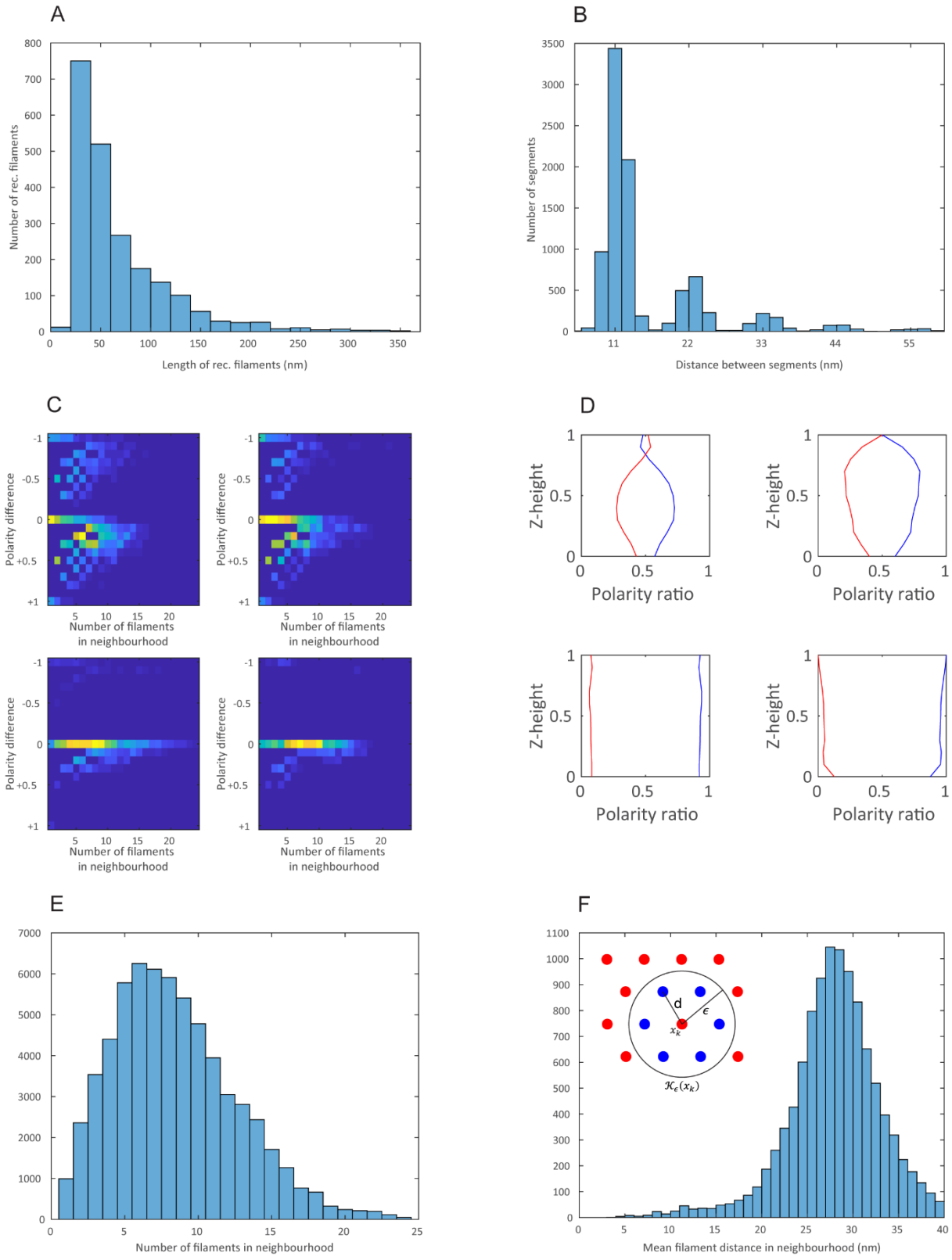

Figure S5. Analysis of actin bundles at FAs. Related to Figure 3. (**A**) Length distribution of reconstructed actin filaments from manual segmented dataset. (**B**) Initially all segments were extracted with an equidistant spacing of 11 nm. However, during 2D classification (*Step V*) a

fraction of segments was rejected, thus the resulting distance distribution between the segments shows peaks located at multiples of 11 nm. (**C**) Using APT's topology module (*Step IX*) the polarity distributions of actin bundles were analyzed. Therefore, the depicted matrices were computed based on the bundles shown in Figure 3E-H (corresponding matrices in the following order: top/left, top/right, bottom/left, and bottom/right). Each matrix element is the number of how often a specific combination of number of filaments within $\mathcal{K}_\epsilon(x_k)$ (x-axis) versus the polarity difference within $\mathcal{K}_\epsilon(x_k)$ (y-axis) appears in a bundle (ϵ=40 nm). High numbers are visualized as yellow/orange matrix elements, the dark blue background indicates zero. All four bundles show a substantial fraction of uniform polarity (polarity difference = 0). However, only in bundles located at proximal regions of FAs (top/left, top/right) a significant amount of mixed polarity neighborhoods can be detected (polarity difference ≠ 0). (**D**) In order to evaluate where mixed polarity regions are localized in the FA actin bundles, we fitted a plane to the bottom of the bundles (the side which is close to the support), and then stepwise moved this plane upwards through the bundle, and recorded for each step the polarity ratio found within the plane. We executed this calculation for the bundles shown in Figure 3E-H. The corresponding plots are shown in the following order: top/left, top/right, bottom/left, and bottom/right. The blue trajectory shows the fraction of filaments that are pointing with their plus-ends towards the cell tip at the respective z-height of the plane, which is plotted normalized between 0 (bottom side of the bundle) and 1 (topside of the bundle). The red trajectory shows the fraction of filaments pointing in the opposite direction at respective z-heights. The two distal bundles with predominantly uniform polarity (bottom/left, bottom/right) show a similar polarity ratio at all z-heights. However, in the two proximal bundles (top/left, top/right) a pronounced mixed polarity can be found mainly at bottom and top side of the bundles. (**E**) During topology analysis (*Step IX*) the number of filaments within $\mathcal{K}_\epsilon(x_k)$ was evaluated. The histogram shows that the most frequent configuration are six neighboring filaments in the FA actin bundles. (**F**) Additionally, the mean distance of the filaments within $\mathcal{K}_\epsilon(x_k)$ was calculated. In the inset a possible packing configuration of the filaments is depicted. Within $\mathcal{K}_\epsilon(x_k)$ the central filament at position x_k is surrounded by six filaments (blue circles) at a distance d of ~28 nm.